SUNDBERG, M. (1978–1979). *Chem. Scr.* **14**, 161–166.
SUNDBERG, M. (1981). *Chem. Commun. Univ. Stockholm*, **5**, 1–53.
SUNDBERG, M. & TILLEY, R. J. D. (1974). *J. Solid State Chem.* **11**, 150–160.
SUNDBERG, M., WERNER, P.-E., ZIBROV, I. P. & LOUËR, D. (1994). In preparation.
TILLEY, R. J. D. (1970). *Mater. Res. Bull.* **5**, 813–824.
TILLEY, R. J. D. (1978–1979). *Chem. Scr.* **14**, 147–159.

Acta Cryst. (1993). B**49**, 958–967

Proton Ordering in the Peierls-Distorted Hydrogen Molybdenum Bronze $H_{0.33}MoO_3$: Structure and Physical Properties

BY STEFAN ADAMS,* KARL-HEINZ EHSES AND JOACHIM SPILKER

Fachbereich Kristallographie der Universität des Saarlandes, D-66041 Saarbrücken, Germany

(*Received* 3 *March* 1993; *accepted* 21 *June* 1993)

Abstract

The intercalation of hydrogen into the layered structure of MoO_3 produces four hydrogen molybdenum bronze phases H_xMoO_3 ($0 < x < 2$). The correlation between the structure and the physical properties of these low-dimensional conductors has been investigated by X-ray diffraction and conductivity measurements. Powder diffraction studies revealed phase transitions as a function of temperature and hydrogen content. A new proton-distribution model describes the lattice distortions resulting from the intercalation in the whole composition range. Superstructure reflections were detected in precession photographs of single crystals of the phases I ($x \simeq 0.3$) and III ($x \simeq 1.6$). A single-crystal structure determination was performed for $H_{0.33}MoO_3$, which exhibits a $3a \times 6c$ superstructure at ambient temperature. Structural and experimental data for this particular composition are: $P_b^2 11$, $a = 11.70$ (1), $b = 14.070$ (5), $c = 22.40$ (2) Å, $\alpha = 90.0$ (1)°, $V = 3687$ (8) Å^3, $Z = 72$, $D_x = 4.68$ (1) Mg m^{-3}, λ(Mo $K\alpha$) = 0.7107 Å, $\mu = 0.593$ cm^{-1}, $F(000) = 4622.6$, $R(F) = 0.10$ for 1223 unique reflections. Valence-sum calculations revealed that all the protons of $H_{0.33}MoO_3$ are located in periodically arranged 6-(OH)-clusters. The long-range proton ordering breaks down at $T_c = 380$ K giving rise to a second-order phase transition. The identification of this transition as a Peierls distortion explains many properties of phase I: conductivity measurements show a metal to non-metal transition at T_c with an unusual temperature dependence of σ in the ordered phase. The multiplication of the unit cell along the c direction as well as T_c depend on the hydrogen content x. The critical exponent of the order parameter $\beta = 0.36$ is compatible with an incommensurate superstructure. Fröhlich conductivity as a result of charge-density-wave depinning is observed in field-dependent conductivity measurements.

Introduction

The hydrogen molybdenum bronzes H_xMoO_3 ($0 < x < 2$) have been the subject of intense studies throughout the last 20 years. Technical interest in the deeply coloured, conducting intercalate phases was raised by a great number of possible applications (*e.g.* hydrogen-transfer catalysts, electrochromic displays, fuel cells, hydrogen storage, gas sensors).

Scientific investigations of the molybdenum bronzes focused on the electronic and ionic charge transport in these mixed low-dimensional conductors. An understanding of the correlations between the structural modifications by intercalation and the distinct changes in the physical properties remained rather limited.

The layered structure of MoO_3 permits the intercalation of protons onto two different types of sites. Protons can occupy places in the van der Waals gaps between the octahedra layers as well as intralayer sites on zigzag chains along the c direction (Fig. 1). Among the four resulting bronze phases, three exist over wide composition ranges (phase I, $0.23 < x < 0.40$; phase II, $0.85 < x < 1.04$; phase III, $1.55 < x < 1.72$). Phase IV, in contrast, proved to be the stoichiometric compound H_2MoO_3 (Birtill & Dickens, 1978).

Powder data

Experimental

Powder samples of phase III were prepared by electrochemical intercalation of hydrogen into

* Present address: Max-Planck-Institut für Festkörperforschung, Heisenbergstrasse 1, D-70569 Stuttgart.

MoO_3. Equilibration of phase III with the appropriate amount of MoO_3 powder yielded samples with lower hydrogen contents (Birtill & Dickens, 1978). The hydrogen content x was controlled by redox titrations following Choain & Marion (1963).

Room-temperature powder data for 34 single-phased samples of phases I–III were collected in the range $10 < 2\theta < 120°$ (Cu $K\alpha$) with a Siemens D500 powder diffractometer. A mylar foil prevented the sample from contact with air.

Thermal expansion data were recorded with a Bragg–Bentano powder diffractometer at a Rigaku Rotaflex rotating anode (Cu $K\alpha$). The samples were mounted in an evacuated cryostat.

Variation of the lattice constants with x

Physically, the lattice constants of the different molybdenum bronze phases are determined by the distribution of protons between the two types of intercalation sites (Ritter, Müller-Warmuth & Schöllhorn, 1985). Therefore, measurements of lattice constants as a function of x within the homogeneity ranges of the individual phases provide a check for the contradictory hydrogen-distribution models discussed in the literature (Dickens, Birtill & Wright, 1979; Ritter, Müller-Warmuth & Schöllhorn, 1985; Bamberg, 1987).

Our data reveal that the changes in the lattice constants do not proceed continuously over the composition ranges of the individual phases. Within phase I the lattice constants show a crossover behaviour at approximately $x = \frac{1}{3}$ (Fig. 2). Furthermore, distinct changes in the slopes of the lattice constant *versus* x curves occur at $x = 0.94$ (phase II) and $x = 1.67$ (phase III) (see Fig. 3).

Such dependences of the lattice constants on x cannot be explained by the published hydrogen-distribution models, which predict a change from intralayer to interlayer intercalation at $x = 0.85$, but no further change of intercalation type up to $x = 2$.

Our results indicate rather that after an almost complete occupation of the intralayer sites (zigzag channels), for $x > 0.94$ additional protons are stored in the van der Waals gap sites and for $x > 1.67$ even those protons, which had previously been intercalated on the intralayer sites, move to the interlayer sites. Consequently, the interlayer sites are com-

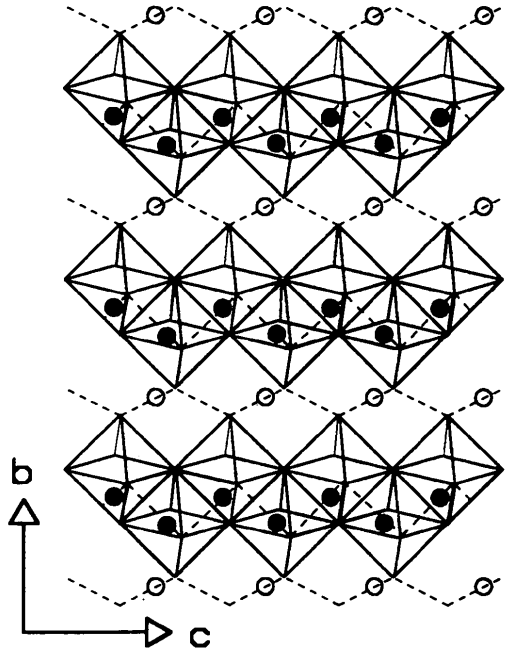

Fig. 1. Possible intercalation sites for hydrogen in MoO_3: ● intralayer positions on zigzag chains along the c direction; ○ interlayer positions in the van der Waals gaps (ac plane).

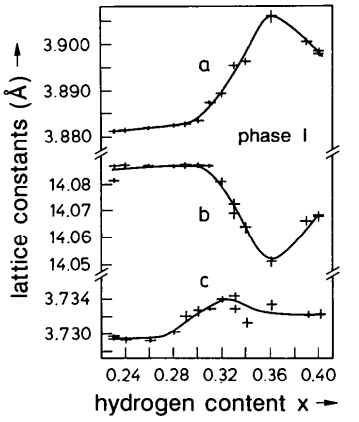

Fig. 2. Variation of the lattice constants with the hydrogen content x within phase I. In the region $0.23 < x < 0.28$, the lattice constants are independent of x. The change in the lattice constants around $x \simeq \frac{1}{3}$ is connected with a rearrangement of the protons (solid line: guideline to the eye).

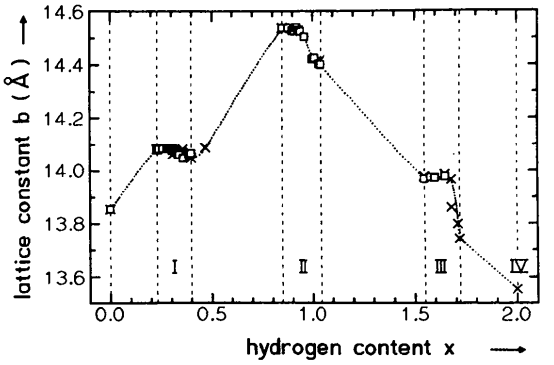

Fig. 3. The lattice constant b as a function of x for all hydrogen molybdenum bronze phases [□, this work; ×, literature data *cf.* Katscher & Schröder (1987); dotted line as a guide to the eye].

pletely filled in the stoichiometric phase IV ($x = 2$), leaving the zigzag chains empty.

As will be seen below, the phase transition in phase I, for which neutron powder diffraction revealed that all the protons reside in the zigzag chains (Schröder & Weitzel, 1977; Dickens, Birtill & Wright, 1979), is correlated with a change in proton ordering. The redistribution of protons within phase III is similarly connected with a breakdown of proton ordering.

Thermal expansion

Thermal expansion coefficients for MoO_3 and the bronze phases I–II were determined from the shifting of about 15 powder Bragg reflections (2θ up to 118°). Powder patterns of phase III, for which a phase transition at 330 K had already been discovered in the specific heat (Bamberg, 1987), were recorded over a wider range of temperatures (130–400 K). The room-temperature thermal expansion coefficients are listed in Table 1.

The thermal expansion coefficient $\alpha_{22} = 45.9 \times 10^{-6}\,K^{-1}$ of MoO_3 along the b direction, in which the octahedra layers are linked only by van der Waals forces, is five times higher than along the a direction with vertex-sharing MoO_6 octahedra ($\alpha_{11} = 9.4 \times 10^{-6}\,K^{-1}$). No thermal expansion could be detected in the c direction, in which the octahedra are connected by common edges.

Earlier data of Kierkegaard (1964) agree only partially with our findings ($\alpha_{11} = 9 \times 10^{-6}\,K^{-1}$, $\alpha_{33} \simeq 0$), but give a value for α_{22} ($180 \times 10^{-6}\,K^{-1}$), which is considerably higher. In contrast, the mean value $\alpha_{22} = 58 \times 10^{-6}\,K^{-1}$ reported by Deb (1968) for the temperature interval 298–773 K is in good accordance with our results, if one considers the temperature dependence of α. The anisotropy of the thermal expansion coefficients corresponds well to the anisotropy of the linear compressibility coefficients given by Åsbrink, Kihlborg & Malinowski (1988).

The thermal-expansion data of the bronze phases can only be discussed in terms of a comparison with our hydrogen-distribution model, since no other reference data are available. The occupation of intralayer sites attenuates the van der Waals attraction between the layers resulting in an increase of both the lattice constant b and α_{22}, whereas the interconnection of the octahedra layers by protons in the van der Waals gap has the opposite effect. For the monoclinic phases, α_{23} decreases with increasing number of interlayer O—H bonds. In all phases with occupied van der Waals sites, α_{11} adopts nearly the same low value thus supporting the model of an additional interaction along the a direction (Anne, Fruchart, Derdour & Tinet, 1988).

Table 1. *Thermal expansion coefficients α_{ij} and volume expansion coefficient β of MoO_3 and the bronze phases*

	MoO_3	Phase I	Phase II	Phase III	Phase IV
H content x	—	0.3	0.85	1.60	2.0
α_{11} ($10^{-6}\,K^{-1}$)	9.4 (0.1)	13.3 (1.0)	3.3 (0.7)	4.6 (0.2)	4.2 (0.5)
α_{22} ($10^{-6}\,K^{-1}$)	45.9 (0.4)	62.2 (0.7)	57.4 (0.8)	−11.2 (0.4)	45 (1)
α_{33} ($10^{-6}\,K^{-1}$)	0.0 (0.3)	−27.5 (0.8)	−5.6 (0.4)	8.1 (0.2)	−3.3 (0.5)
α_{23} ($10^{-6}\,K^{-1}$)	—	—	23.8 (0.2)	−3.5 (0.2)	−5 (1)
β ($10^{-6}\,K^{-1}$)	55.3 (0.8)	48 (3)	55 (2)	1.5 (0.8)	46 (3)

Below T_c, a spontaneous deformation appears in all bronze phases (*e.g.* in phase III, *cf.* Fig. 4). In phase IV, the curvature of the α *versus* T diagram indicates a transition slightly above the decomposition temperature. MoO_3 does not show a comparable transition. In the bronze phases T_c diminishes with increasing hydrogen content, illustrating the strong correlation of these transitions with intercalation. In analogy to the phase transitions as a function of x we identify the transition in phase I with a breakdown of proton ordering. For the phases II and IV the transitions represent a migration of protons from the zigzag chains to the van der Waals gaps or *vice versa*, and in phase III both proton distribution and proton order are presumed to change at T_c.

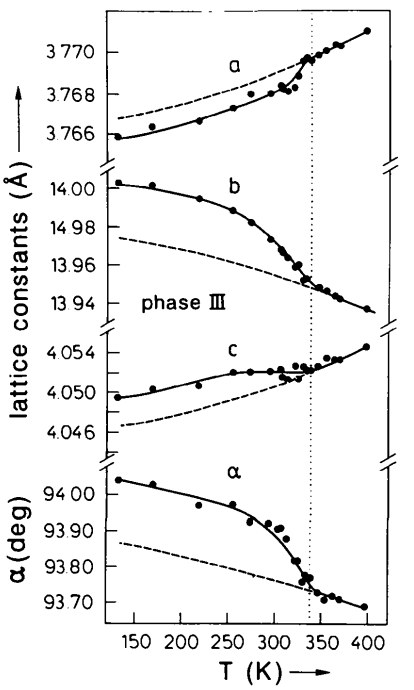

Fig. 4. Temperature dependence of the lattice constants in a powder sample of phase III ($x \simeq 1.60$), revealing a phase transition at $T_c \simeq 335$ K (solid line: fitted curve). The difference between the solid line and the dotted line corresponds to the spontaneous deformation.

Single-crystal data

Experimental

Single crystals of MoO_3 have been converted into homogeneous single crystals of the phases I–III for X-ray investigations and conductivity measurements. The procedure which involves a modified spillover process and reduction in a solid-state electrochemical cell has been described elsewhere (Adams, Ehses & Schwitzgebel, 1991).

The homogeneity of the crystals was confirmed by precession photographs. A comparison of the single-crystal lattice constants with our calibration curves from powder diffraction (see Fig. 2) enabled us to determine the hydrogen content without destruction of the sample.

A single-crystal structure analysis was carried out for an $H_{0.33}MoO_3$ single crystal ($0.42 \times 0.10 \times 0.025$ mm) on an automatic single-crystal diffractometer (AED, Philips): Mo $K\alpha$ radiation, lattice constants determined from 25 reflections up to $\theta = 39°$, 3314 observed reflections with $I > \sigma$ from two data sets (2θ–θ scan). Data set I: 754 'strong' main reflections and 366 'weak' main reflections (*cf.* Fig. 5) up to $\sin\theta/\lambda = 1.08$ Å^{-1}, 576 satellite reflections up to $\sin\theta/\lambda = 0.62$ Å^{-1}; data set II: 1150 'strong' and 468 'weak' main reflections up to $\sin\theta/\lambda = 0.76$ Å^{-1} (same crystal, but extended counting time for the weak reflections). An absorption correction was performed with the program *DATAPH* (Coppens, 1968). No extinction correction was made.

Starting atomic coordinates for the refinement of the mean structure were taken from Wilhelmi (1969) and scattering factors f', f'' from *International Tables for X-ray Crystallography* (1974, Vol. IV).

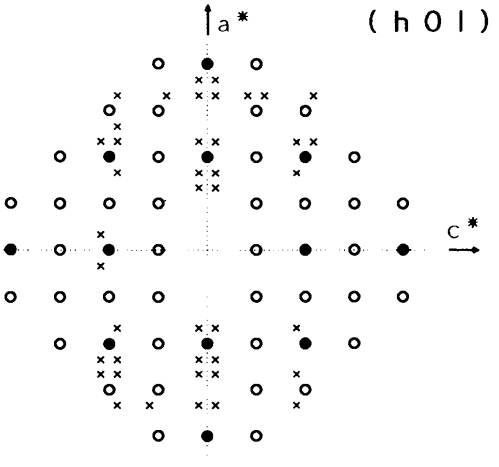

Fig. 5. Idealized precession photograph of the *h0l* plane in $H_{0.33}MoO_3$. ● main reflections, allowed in *Cmcm*. ○ weak reflections, not allowed in *Cmcm*. × satellite reflections, displaying a $3a \times 6c$ superstructure.

Least-squares calculations were performed with the program *BLFLS*, which is based on *ORXFLS*3 (Busing, Martin & Levy, 1974). Refinement proceeded until the following residuals were obtained (all refinements based on *F*): $R = 0.066$, $wR = 0.069$ for the mean structure from 485 unique 'strong main reflections' ($R_{Int} = 0.063$); $R = 0.10$, $wR = 0.13$, $S = 1.65$ for the modulated structure (largest shift in final cycle $< 0.06\sigma$).

Proton ordering in phases I and III

Precession photographs of our phase I single crystals (Fig. 5) show the assignment of the space group *Cmcm*, as given in the literature, to be incorrect (Wilhelmi, 1969). Numerous weak reflections (open circles in Fig. 5) violate the integral extinction rule of *Cmcm*, but are compatible with the space group $P2_1/b11$ (No. 14). This non-standard setting of $P2_1/c$ preserves the choice of axes in the host structure MoO_3. A deviation of the monoclinic angle α from orthogonality was not detected.

Photographs with long exposure times (*ca* 7 d) showed additional satellite reflections (crosses in Fig. 5). For a crystal with $x = \frac{1}{3}$ the modulation represents a $3a \times 6c$ superstructure. Crystals with the slightly lower hydrogen content $x = 0.30$ exhibit a higher multiplication of the lattice constant c ($c' = 6.7 \times c$). The superstructure reflections vanish in a second-order phase transition at $T_c = 380$ K (Fig. 6). The proton ordering below T_c causes the spontaneous lattice deformation found in the thermal expansion measurements (see above). Those 'weak' reflections that are inconsistent with *Cmcm* are extinguished above T_c. It is noteworthy that a second-order transition from *Cmcm* to $P2_1/b11$ is forbidden according to Landau theory.

* A list of structure factors has been deposited with the British Library Document Supply Centre as Supplementary Publication No. SUP 71274 (23 pp.). Copies may be obtained through The Technical Editor, International Union of Crystallography, 5 Abbey Square, Chester CH1 2HU, England.

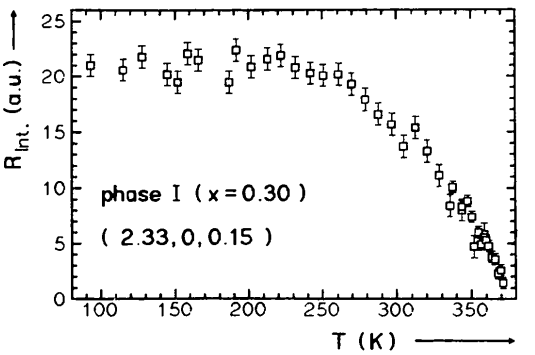

Fig. 6. Integrated intensity R_{Int} of the superstructure reflection (2.33, 0, 0.15) in arbitrary units as a function of temperature for a $H_{0.30}MoO_3$ single crystal.

Satellite reflections have also been detected in precession photographs of phase III single crystals, where they display the existence of a $2a \times 2c$ superstructure. No indications of a superstructure were found for crystals of phase II.

Structure analysis of $H_{0.33}MoO_3$

The three classes of reflections reveal different aspects of the structure. The 'strong' main reflections, *i.e.* those reflections that are allowed in *Cmcm*, determine the mean structure of the subcell. The 'weak' main reflections, which violate the extinction rules of *Cmcm*, describe the small deviations of all atoms from the cancelled mirror plane at $x = 0$. Finally, the satellite reflections contain information about the modulation of the atomic positions in the $3a \times 6c$ superstructure.

In a first step we only considered the 485 'strong' main reflections with $\sin\theta/\lambda < 1.08$ Å^{-1}. Assuming the space group *Cmcm*, a refinement of these data [$wR(F) = 0.069$] yielded virtually the same atomic parameters as the earlier single-crystal structure determination by Wilhelmi (1969) and the two neutron powder studies (Schröder & Weitzel, 1977; Dickens, Birtill & Wright, 1979). But like these authors we found unreasonably high formal temperature factors, which we ascribed to a projection of the structure modulation into the subcell. From the refinement of anisotropic temperature factors we concluded that the structure modulation should predominantly affect the x coordinate of the Mo atoms and the y coordinate of the O(2) atoms.

The inclusion of the 'weak' main reflections and of the satellite reflections then permitted a refinement of the modulated structure (see Table 2).

Thereby, the formal temperature factors were reduced by a factor of up to 3 compared to the mean structure (Table 3). Moreover, the differences between the temperature factors for the O atoms, the values of which ranged from $B = 0.45$ to 2.66 Å^2 in Wilhelmi's refinement (1969), narrow significantly.

As only first-order satellites of the type $h \pm 1\, k\, l \pm 1$ were found, the refinement was restricted to the phases φ and amplitudes Δ of the structure modulations, which were taken as sinusoidal (see Table 4).

For all types of atoms the atom numbers 7–12 (13–18) mean a shift of $\frac{1}{3}$ ($\frac{2}{3}$) in their x coordinate compared to the atoms 1–6. The introduction of an additional displacement δ for the mean x values of Mo(7–12) and $-\delta$ for Mo(13–18), which are interrelated by symmetry, considerably improved the refinement. Thus, the applied modulation function for the Mo atoms $i = 7$–12 runs

$$x(\mathrm{Mo},i) = \bar{x}(\mathrm{Mo}) + (\tfrac{1}{3} + \delta) + \Delta(\mathrm{Mo}) \cdot \sin[2\pi z(\mathrm{Mo},i) + \varphi]. \quad (1)$$

Table 2. *Atomic coordinates of the modulated* $H_{0.33}MoO_3$ *structure*

	x	y	z		x	y	z
Mo(1)	0.0112	0.1034	0.0417	O(2,1)	0.1680	0.0834	0.0417
Mo(2)	0.0179	0.1034	0.2083	O(2,2)	0.1680	0.0911	0.2083
Mo(3)	0.0155	0.1034	0.3750	O(2,3)	0.1680	0.0883	0.3750
Mo(4)	0.0063	0.1034	0.5417	O(2,4)	0.1680	0.0778	0.5417
Mo(5)	−0.0004	0.1034	0.7083	O(2,5)	0.1680	0.0702	0.7083
Mo(6)	0.0021	0.1034	0.8750	O(2,6)	0.1680	0.0730	0.8750
Mo(7)	0.3431	0.1034	0.0417	O(2,7)	0.5013	0.0911	0.0417
Mo(8)	0.3364	0.1034	0.2083	O(2,8)	0.5013	0.0911	0.2083
Mo(9)	0.3388	0.1034	0.3750	O(2,9)	0.5013	0.0911	0.3750
Mo(10)	0.3480	0.1034	0.5417	O(2,10)	0.5013	0.0911	0.5417
Mo(11)	0.3547	0.1034	0.7083	O(2,11)	0.5013	0.0911	0.7083
Mo(12)	0.3522	0.1034	0.8750	O(2,12)	0.5013	0.0911	0.8750
Mo(13)	0.6696	0.1034	0.0417	O(2,13)	0.8346	0.0778	0.0417
Mo(14)	0.6629	0.1034	0.2083	O(2,14)	0.8346	0.0702	0.2083
Mo(15)	0.6653	0.1034	0.3750	O(2,15)	0.8346	0.0730	0.3750
Mo(16)	0.6745	0.1034	0.5417	O(2,16)	0.8346	0.0834	0.5417
Mo(17)	0.6812	0.1034	0.7083	O(2,17)	0.8346	0.0911	0.7083
Mo(18)	0.6787	0.1034	0.8750	O(2,18)	0.8346	0.0883	0.8750
O(1,1)	−0.0025	0.0655	0.1250	O(3,1)	0.0081	0.2212	0.0417
O(1,2)	−0.0025	0.0655	0.2917	O(3,2)	0.0050	0.2212	0.2083
O(1,3)	−0.0025	0.0655	0.4583	O(3,3)	0.0061	0.2212	0.3750
O(1,4)	−0.0025	0.0655	0.6250	O(3,4)	0.0104	0.2212	0.5417
O(1,5)	−0.0025	0.0655	0.7917	O(3,5)	0.0136	0.2212	0.7083
O(1,6)	−0.0025	0.0655	0.9583	O(3,6)	0.0124	0.2212	0.8750
O(1,7)	0.3308	0.0655	0.1250	O(3,7)	0.3438	0.2212	0.0417
O(1,8)	0.3308	0.0655	0.2917	O(3,8)	0.3469	0.2212	0.2083
O(1,9)	0.3308	0.0655	0.4583	O(3,9)	0.3457	0.2212	0.3750
O(1,10)	0.3308	0.0655	0.6250	O(3,10)	0.3414	0.2212	0.5417
O(1,11)	0.3308	0.0655	0.7917	O(3,11)	0.3383	0.2212	0.7083
O(1,12)	0.3308	0.0655	0.9583	O(3,12)	0.3394	0.2212	0.8750
O(1,13)	0.6642	0.0655	0.1250	O(3,13)	0.6771	0.2212	0.0417
O(1,14)	0.6642	0.0655	0.2917	O(3,14)	0.6802	0.2212	0.2083
O(1,15)	0.6642	0.0655	0.4583	O(3,15)	0.6791	0.2212	0.3750
O(1,16)	0.6642	0.0655	0.6250	O(3,16)	0.6748	0.2212	0.5417
O(1,17)	0.6642	0.0655	0.7917	O(3,17)	0.6716	0.2212	0.7083
O(1,18)	0.6642	0.0655	0.9583	O(3,18)	0.6728	0.2212	0.8750

Table 3. *Final anisotropic temperature factors* (Å^2) *and standard deviations* (*in parentheses*) *as obtained from the least-squares refinement*

	U_{11}	U_{22}	U_{33}	U_{12}	U_{13}	U_{23}
Mo	0.0099	0.0091	0.0048	−0.0013	−0.0001	−0.0002
	(0.0004)	(0.0003)	(0.0004)	(0.0004)	(0.0004)	(0.0003)
O(1)	0.0210	0.0130	0.0045	0.0061	−0.0021	−0.0008
	(0.0027)	(0.0024)	(0.0029)	(0.0083)	(0.0115)	(0.0026)
O(2)	0.0174	0.0150	0.0142	0.0018	0.0062	0.0007
	(0.0033)	(0.0038)	(0.0042)	(0.0178)	(0.0145)	(0.0038)
O(3)	0.0169	0.0129	0.0133	−0.0040	0.0026	0.0005
	(0.0033)	(0.0024)	(0.0036)	(0.0034)	(0.0042)	(0.0029)

A separate modulation amplitude for the y coordinate of the O(2) atoms 7–12 refined to zero with the mean value oscillating around the maximum y coordinate for the other rows of O(2) atoms. Therefore, y[O2(7–12)] was restricted to this value in the final refinement cycles.

Fig. 7 shows an *ORTEP*II plot (Johnson, 1976) of the refined superstructure for $H_{0.33}MoO_3$. The transversal displacements of the Mo atoms in the Mo—O(1) chains [Δx(Mo) = 0.11 Å] result in the formation of four regions with enlarged Mo—O(2)—Mo distances along the a direction (Fig. 8*a*). The modulation in the y coordinate of the affected O(2) atoms [Δy(O2) = 0.15 Å] reduces the O(2)—O(2) distances along the zigzag chains (2.72–2.94 Å in these regions compared to the normal value of 3.17 Å) because of hydrogen bonds between these atoms (Fig. 8*b*).

Table 4. *Refined parameters with e.s.d.'s in parentheses (values without e.s.d.'s not refined)*

$\bar{x}$(Mo)	0.00879 (0.00006)
y(Mo)	0.10341 (0.00004)
z(Mo,i)	[0.25000 + (i − 1)](1/6)
x(O1)	−0.00250 (0.00046)
y(O1)	0.06546 (0.00037)
z(O1,i)	[0.75000 + (i − 1)](1/6)
x(O2)	0.16796 (0.00046)
$\bar{y}$(O2)	0.08063 (0.00047)
y[O2(7–12)]	0.09108 = max. [y(O2)]
z(O2,i)	[0.25000 + (i − 1)](1/6)
$\bar{x}$(O3)	0.00926 (0.00050)
y(O3)	0.22120 (0.00043)
z(O3,i)	[0.25000 + (i − 1)](1/6)
Amplitudes of the modulations	
Δx(Mo)	0.00948 (0.00008)
Δy(O2)	0.01082 (0.00088)
Δx(O3)	−0.00445 (0.00069)
Additional displacement in the x coordinate of the chains	
O(1,7–12), O(2,7–12), O(3,7–12)	$\frac{1}{3}$
O(1,13–18), O(2,13–18), O(3,13–18)	$\frac{2}{3}$
Mo(7–12)	$\frac{1}{3}$ + 0.00342 (0.00020)
Mo(13–18)	$\frac{2}{3}$ − 0.00342 (0.00020)
Phases φ (°) of the modulations for z = 0 in the chains	
Mo(1–6)	0
O(2,1–6), O(3,1–6)	0
Mo(7–12), Mo(13–18)	180
O(2,13–18)	180
O(3,7–12), O(3,13–18)	180

Localization of protons

A direct determination of the proton intercalation sites by neutron diffraction was impossible, because homogeneous single crystals of phase I with the required dimensions could not be grown.

The proton intercalation sites were deduced indirectly from the distortion of the host structure by means of the empirical bond-length–bond-strength relation for Mo—O bonds

$$s(\text{Mo—O}) = \left[\frac{1.882\ \text{Å}}{R(\text{Mo—O})}\right]^6, \qquad (2)$$

where R = bond length, s = bond strength (Brown & Wu, 1976). This relation is valid for Mo atoms with valence states from Mo^{II} to Mo^{VI} (Bart & Ragaini, 1979). Thus, it can be applied to the hydrogen molybdenum bronzes, where the valence of the individual Mo in the superstructure is *a priori* unknown, but surely within the allowed range.

The calculation of valence sums W(O),

$$W(\text{O}) = \Sigma s(\text{Mo—O}), \qquad (3)$$

for all O atoms confirms earlier findings from NMR and neutron powder diffraction studies that all the protons of $H_{0.33}MoO_3$ occupy intralayer sites along the O(2)-zigzag chains and that none of the O(2) atoms is directly bound to more than one proton (no H_2O groups!). In contrast to the published powder structure refinements (Dickens, Birtill & Wright, 1979; Schröder & Weitzel, 1977), we found that the distribution of protons on the intralayer sites is not random.

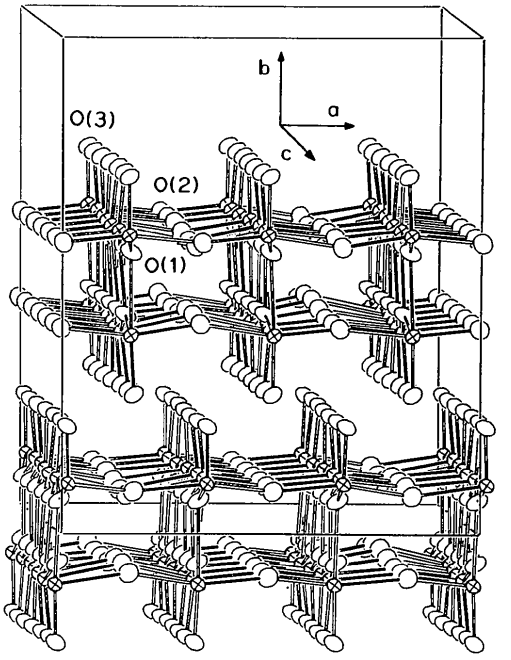

Fig. 7. *ORTEP*II plot of the $3a \times 6c$ superstructure of $H_{0.33}MoO_3$ with the different modulations of the Mo (⊗) and O atoms (○).

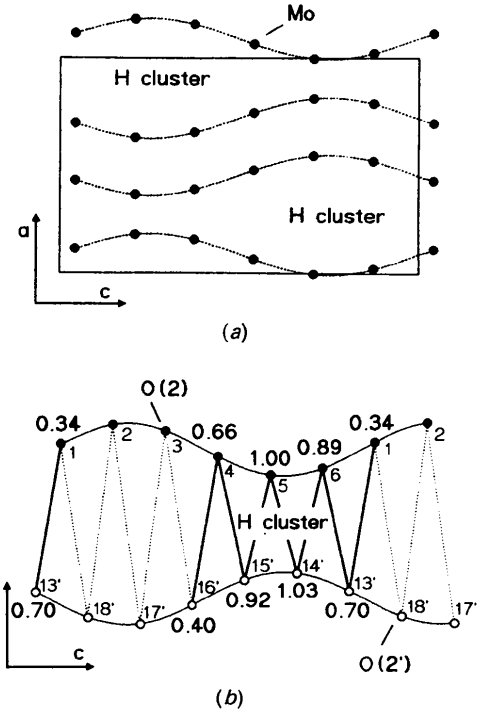

Fig. 8. (*a*) Modulation of the Mo atoms in one of the two *ac* planes. (*b*) Modulation of the O(2) atoms in the *bc* plane. The numbers indicate the site occupancy of the protons in the cluster according to valence-sum calculations.

Deviations from a statistical proton distribution in phase I had in fact been noticed earlier in powder H NMR studies, but were interpreted as a short-range ordering, namely the preferred formation of pairs of OH groups (Slade, Halstead & Dickens, 1980) or clusters of 3 OH groups (Ritter, Müller-Warmuth, Spiess & Schöllhorn, 1982).

The bond-length–bond-strength approach applied here reveals a long-range ordering of the protons consisting of a periodic arrangement of 6-(OH)-clusters. As shown schematically in Fig. 8(*a*), two of every three neighbouring zigzag chains within the same MoO_3 layer are half filled with proton clusters at their maximum separation, while the third chain contains no protons.

The number of protons localized in the four 6-(OH)-clusters per unit cell accounts for the total hydrogen content x. Thus, the protons in $H_{0.33}MoO_3$ are completely ordered.

From the O(2)—O(2) distances (Pimentel & McClellan, 1960) and the application of a bond-length–bond-strength relationship for O—H bonds (Brown, 1981), the O—H bond distance can be roughly estimated at 1.05 Å in accordance with the result of Dickens (1.09 Å), but considerably smaller than the value given by Schröder (1.3 Å).

The calculation of valence sums for the Mo atoms indicates that the electron of the H atom is essentially transferred to the adjacent Mo atom with the elongated Mo—O(2) bond. This electron localization seems remarkable, since calculations by Travaglini & Wachter (1983) predict the formation of a one-dimensional conduction band by d_π–p_π orbital overlap as a result of the short bond distances along the Mo—O(1) chains.

Peierls transition in phase I

Regarding phase I as a quasi-one-dimensional conductor provides an explanation for the observed physical and structural properties. At low temperatures one-dimensional metals are unstable against a periodic lattice distortion that opens an energy gap at the Fermi level (Peierls, 1955). The amplitude of either the structural modulation or the band gap can be chosen as the order parameter η.

The period c' of the structural modulation depends on the number of electrons in the conduction band of the metallic high-temperature phase

$$c' = (2/n) \times c, \qquad (4)$$

where n is the number of electrons in the conduction band per energy level and c is the lattice constant of the undistorted structure.

Generally, c' is incommensurate to the underlying lattice. The weak interactions of neighbouring chains in layered structures lead to two-dimensional superstructures with commensurate cell multiplications perpendicular to the chains, while the new lattice constant in the chain direction follows equation (4).

For phase I this equation yields the crystallographically observed lattice constant c'.

$$c' = (2/0.33) \times c = 6 \times c, \qquad (5)$$

if one supposes a complete electron transfer from the H atom to the conduction band ($n = x$); a lower hydrogen content results in higher cell multiplication, as seen in our precession photographs (see above).

Conductivity measurements

Direct evidence for the existence of a Peierls transition in phase I comes from conductivity measurements that reveal a metal to semiconductor transition for powder as well as single-crystal samples (Fig. 9). The a.c. conductivity measurements were performed in an evacuated cryostat. Single crystals were contacted along their c direction with silver paint.

The conductivity remains nearly constant in the temperature interval between the transition temperature and the decomposition temperature ($\simeq$420 K). Below T_c, the conductivity rapidly decreases. T_c was found to decrease with increasing hydrogen content of the sample from 415 to 375 K. Because of a small loss of hydrogen in the heating run, T_c is slightly increased in the subsequent cooling run.

Assuming that the ordered phase I is a normal semiconductor, the temperature dependence of the thermal activation energy ΔE (energy distance between Fermi level and conduction band) can be calculated from our measurements according to the Arrhenius equation

$$\sigma = \sigma_0 \exp(-\Delta E/kT) \qquad (6)$$

(*cf.* Fig. 10).

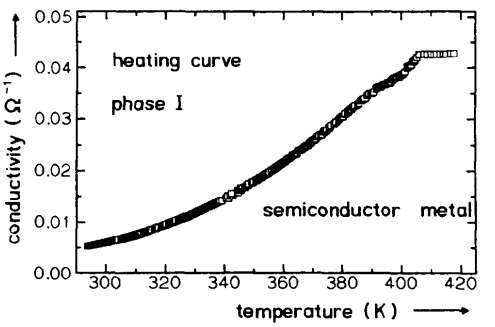

Fig. 9. A.c. conductivity (ν = 1 kHz, $\tilde{U}$ = 200 mV) of a powder sample of phase I ($x \simeq 0.3$), illustrating the metal-to-semiconductor transition.

At lower temperatures the temperature dependence of the conductivity σ deviates from an Arrhenius-type behaviour (Barbara, Gammie, Lyding & Jonas, 1988). A more appropriate description is achieved by a power law,

$$\sigma \sim T^m, \tag{7}$$

with an exponent $m \simeq 7$.

This subactivated behaviour, which has previously been observed in several other charge-density-wave (CDW) systems (Horn & Guidotti, 1977), is attributed to electron-hopping processes between bound solitons. With decreasing temperature the contribution of this hopping process to the total conductivity becomes more and more important (Kivelson, 1982; Su, Schrieffer & Heeger, 1980).

In incommensurate CDW systems a sinusoidal CDW has no preferred position with respect to the lattice. Thus, no activation energy is needed for charge transport by a collective motion of the CDW (Fröhlich, 1954). In real systems the CDW's are localized at pinning centres, particularly at lattice defects.

An increase of the conductivity at ambient temperature as a result of CDW depinning is observed for phase I single crystals when the external electric field E exceeds a threshold value $E_T \simeq 500$–$700\ \mathrm{mV\ cm^{-1}}$ (Fig. 11). E_T depends on the temperature, the quality of the samples and on contact preparations. Application of low-frequency a.c. voltage ($\nu = 1$ kHz) prevents a decomposition of the sample, which causes a conductivity drop at high voltages in the d.c. experiments.

The specific excess conductivity σ_{CDW} follows an empirical relationship given by Mihály, Beauchêne, Marcus, Dumas & Schlenker (1988):

$$\sigma_{\mathrm{CDW}} \sim \sigma_{\mathrm{normal}}\,(E_T/E)[(E/E_r) - 1]^{\alpha}. \tag{8}$$

The uncertainty in the measured conductivity is mainly a result of oscillations in the current response to a voltage change. After the external field has been switched off, several hours are required until the conductivity returns to its initial value. Both effects are ascribed to transitions among the metastable states in which a CDW can be pinned (Schlenker, Dumas, Escribe-Filippini & Guyot, 1989; Fleming & Cava, 1989).

The field dependence of the conductivity yields a possible explanation for peaks below T_c in our ΔE *versus* T curves (see Fig. 10). The amplitude of the voltage was fixed to 200 mV in the temperature-dependent conductivity measurements to avoid a CDW depinning. When E_T decreases below this value in the vicinity of T_c, the excess conductivity as a result of moving CDW's simulates a sudden rise of ΔE.

Critical behaviour at T_c

The critical exponent β of the order parameter η provides a further criterion for the existence of an incommensurate superstructure. The Landau theory for second-order phase transitions yields $\beta = 0.5$, whereas the three-dimensional XY model, which often applies to incommensurate phases, gives $\beta = 0.345$.

The critical exponent β can be determined from our measurements in three independent ways. The integrated intensity of the satellite reflections in the ordered low-temperature phase is proportional to η^2. A log–log representation of the integrated intensity *versus* the reduced temperature $t = (T_c - T)/T_c$ in the vicinity of the phase transition of phase I exhibits the slope $2\beta = 0.72 \pm 0.03$ (Fig. 12).

An analogous diagram for the relationship between the spontaneous deformation (from our

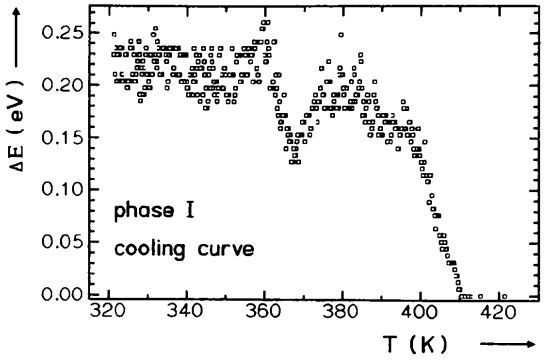

Fig. 10. Temperature dependence of the thermal activation energy ΔE calculated from conductivity measurements in a powder sample of phase I ($x \simeq 0.3$) with the transiton to the semiconducting state at $T_c = 410$ K. The dip at 370 K is discussed in the text.

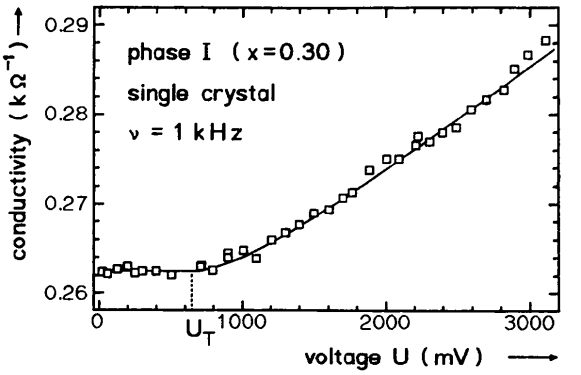

Fig. 11. A.c. conductivity in the c direction of an $H_{0.30}MoO_3$ single crystal (crystal length 1 cm) *versus* the applied voltage. The solid line above U_T represents a fit of the excess conductivity according to equation (7).

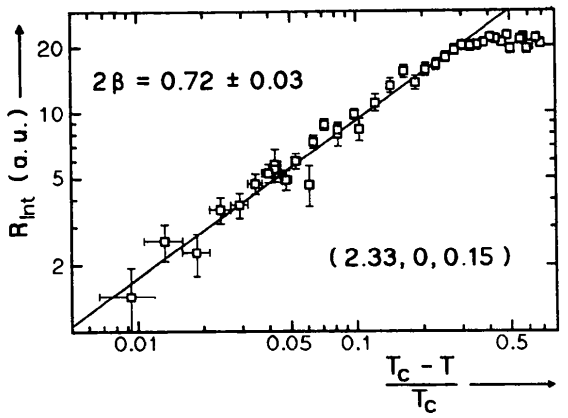

Fig. 12. Log–log representation of the integrated satellite intensity (*cf.* Fig. 5) *versus* the reduced temperature $t = (T_c - T)/T_c$, yielding a critical exponent $2\beta = 0.72 \pm 0.03$.

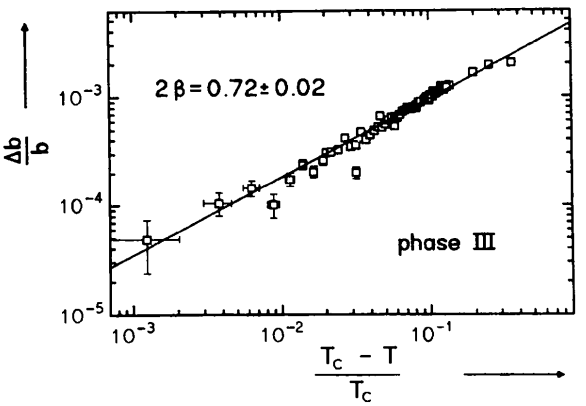

Fig. 13. Log–log representation of the spontaneous deformation $\Delta b/b$ *versus* the reduced temperature $t = (T_c - T)/T_c$ in phase III ($x = 1.6$). In phase III we obtain nearly the same critical exponent $2\beta = 0.72 \pm 0.02$ as in phase I.

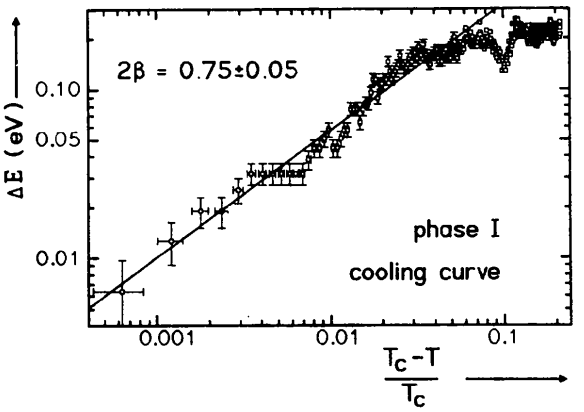

Fig. 14. The temperature dependence of the gap energy ΔE in phase I is determined by a critical exponent $2\beta = 0.75 \pm 0.05$.

powder data) and the reduced temperature corroborates this result also for phase III, which we suppose to be a two-dimensional Peierls system (Fig. 13).

Finally, the temperature dependence of the band gap energy, known from the conductivity measurements in the ordered phase, yields $2\beta = 0.75 \pm 0.05$ (Fig. 14).

Conclusions and prospects

The discovery of additional phase transitions as a function of temperature and hydrogen content demonstrates the complexity of the phase diagram for the hydrogen molybdenum bronzes. The determination of the complete phase diagram is a priority task to elucidate the inter-relationships between the two classes of phase transitions.

The description of phase I as a quasi-one-dimensional conductor, susceptible to a Peierls distortion, adequately explains the structural and physical consequences of hydrogen intercalation.

In phase III, where the protons partly occupy the van der Waals gap (*ac* plane), the Mo—O distances along both the *a* and *c* direction fulfil the Travaglini criterion for electron delocalization (Travaglini & Wachter, 1983). A similar situation is assumed for phase IV. Such two-dimensional conductors, which remain metallic below their Peierls transition, are candidates for superconductivity (Wilson, Di Salvo & Mahajan, 1975; Whangbo & Canadell, 1989; Escribe-Filippini, Beille, Boujida, Marcus & Schlenker, 1989).

The electronic properties of H_xMoO_3 resemble those of the diverse alkali molybdenum bronzes, among which are several 'classical oxide superconductors', despite the considerable structural differences (Greenblatt, McCarroll, Neifeld, Croft & Waszczak, 1984; Raub, 1988).

The availability of single crystals, in which the dimensionality of electronic as well as ionic conduction can be adjusted by the hydrogen content, allows the hydrogen molybdenum bronzes to serve as model systems for the investigation of low-dimensional conductors.

We thank G. Schwitzgebel, H. Schmitt and J. Aschenbach for their valuable cooperation. The financial support of the Deutsche Forschungsgemeinschaft is gratefully acknowledged.

References

ADAMS, ST., EHSES, K. H. & SCHWITZGEBEL, G. (1991). *Synth. Met.* **43**, 3953–3956.

ANNE, M., FRUCHART, D., DERDOUR, S. & TINET, D. (1988). *J. Phys. Fr.* **49**, 505–509; erratum (1988). **49**, 1315.

ÅSBRINK, S., KIHLBORG, L. & MALINOWSKI, M. (1988). *J. Appl. Cryst.* **21**, 960–962; erratum (1989). **22**, 380.
BAMBERG, J. (1987). Thesis, Saarbrücken, Germany.
BARBARA, T. M., GAMMIE, G., LYDING, J. W. & JONAS, J. (1988). *J. Solid State Chem.* **75**, 183–187.
BART, J. C. J. & RAGAINI, V. (1979). *Inorg. Chim. Acta*, **36**, 261–265.
BIRTILL, J. J. & DICKENS, P. G. (1978). *Mater. Res. Bull.* **13**, 311–316.
BROWN, I. D. (1981). *Structure and Bonding in Crystals*, Vol. II, edited by M. O'KEEFFE & A. NAVROTSKY, pp. 1–30. New York: Academic Press.
BROWN, I. D. & WU, K. K. (1976). *Acta Cryst.* B**32**, 1957–1959.
BUSING, W. R., MARTIN, K. D. & LEVY, H. A. (1974). *ORXFLS3*. Oak Ridge National Laboratory, Tennessee, USA.
CHOAIN, C. & MARION, F. (1963). *Bull. Soc. Chim. Fr.* p. 212.
COPPENS, P. (1968). *DATAPII*. SUNY, Buffalo, USA.
DEB, S. K. (1968). *Proc. R. Soc. London Ser. A*, **304**, 211–231.
DICKENS, P. G., BIRTILL, J. J. & WRIGHT, C. J. (1979). *J. Solid State Chem.* **28**, 185–193.
ESCRIBE-FILIPPINI, C., BEILLE, J., BOUJIDA, M., MARCUS, J. & SCHLENKER, C. (1989). *Physica*, C**162–164**, 427–428.
FLEMING, R. M. & CAVA, R. J. (1989). *Low-Dimensional Electronic Properties of Molybdenum Bronzes and Oxides*, edited by C. SCHLENKER, pp. 259–294. Dordrecht: Kluwer Academic Publishers.
FRÖHLICH, H. (1954). *Proc. R. Soc. London Ser. A*, **223**, 296–305.
GREENBLATT, M., MCCARROLL, W. H., NEIFELD, R., CROFT, M. & WASZCZAK, J. V. (1984). *Solid State Commun.* **51**, 671–674.
HORN, P. M. & GUIDOTTI, D. (1977). *Phys. Rev. B*, **16**, 491–501.
JOHNSON, C. K. (1976). *ORTEPII*. Report ORNL-5138. Oak Ridge National Laboratory, Tennessee, USA.
KATSCHER, H. & SCHRÖDER, F. (1987). Editors. *Gmelin Handbook of Inorganic Chemistry*, 8th ed., Mo Suppl., Vol. B3*a*, pp. 11–12. Berlin: Springer-Verlag.
KIERKEGAARD, P. (1964). *Ark. Kemi* **23**, 223–226.
KIVELSON, S. (1982). *Phys. Rev. B*, **25**, 3798–3821.
MIHÁLY, G., BEAUCHÊNE, P., MARCUS, J., DUMAS, J. & SCHLENKER, C. (1988). *Phys. Rev. B*, **37**, 1047–1050.
PEIERLS, R. E. (1955). *Quantum Theory of Solids*, p. 108. Oxford Univ. Press.
PIMENTEL, G. C. & MCCLELLAN, A. L. (1960). *The Hydrogen Bond*, p. 259. San Francisco: Freeman.
RAUB, C. J. (1988). *J. Less-Common Met.* **137**, 287–295.
RITTER, C., MÜLLER-WARMUTH, W. & SCHÖLLHORN, R. (1985). *J. Chem. Phys.* **83**, 6130–6138.
RITTER, C., MÜLLER-WARMUTH, W., SPIESS, H. W. & SCHÖLLHORN, R. (1982). *Ber. Bunsenges. Phys. Chem.* **86**, 1101.
SCHLENKER, C., DUMAS, J., ESCRIBE-FILIPPINI, C. & GUYOT, H. (1989). *Low-Dimensional Electronic Properties of Molybdenum Bronzes and Oxides*, edited by C. SCHLENKER, pp. 159–257. Dordrecht: Kluwer Academic Publishers.
SCHRÖDER, F. A. & WEITZEL, H. (1977). *Z. Anorg. Allg. Chem.* **435**, 247–256.
SLADE, R. C. T., HALSTEAD, T. K. & DICKENS, P. G. (1980). *J. Solid State Chem.* **34**, 183–192.
SU, W. P., SCHRIEFFER, J. R. & HEEGER, A. J. (1980). *Phys. Rev. B*, **22**, 2099.
TRAVAGLINI, G. & WACHTER, P. (1983). *Solid State Commun.* **47**, 217–221.
WHANGBO, M.-H. & CANADELL, E. (1989). *Acc. Chem. Res.* **22**, 375–381.
WILHELMI, K. A. (1969). *Acta Chem. Scand.* **23**, 419–428.
WILSON, J. A., DI SALVO, F. J. & MAHAJAN, S. (1975). *Adv. Phys.* **24**, 117–201.

Acta Cryst. (1993). B**49**, 967–973

Accurate Synchrotron Radiation $\Delta\rho$ Maps for K_2SiF_6 and K_2PdCl_6

BY J. R. HESTER, E. N. MASLEN AND N. SPADACCINI

Crystallography Centre, University of Western Australia, Crawley 6009, *Australia*

N. ISHIZAWA

Research Laboratory of Engineering Materials, Tokyo Institute of Technology, 4259 *Nagatsuta, Midori-Ku, Yokohama* 227, *Japan*

AND Y. SATOW

Faculty of Pharmaceutical Sciences, University of Tokyo, Hongo 7-3-1, *Bunkyo-ku, Tokyo* 113, *Japan*

(*Received* 1 *December* 1992; *accepted* 7 *June* 1993)

Abstract

Difference electron densities for the structurally isomorphic title compounds have been measured using 0.9 and 0.7 Å synchrotron radiation as well as Mo $K\alpha$ ($\lambda = 0.71069$ Å) radiation. The merits of using synchrotron radiation for such accurate electron density studies are confirmed. The noise level in the 0.9 Å K_2SiF_6 $\Delta\rho$ maps is low, and justifies confidence in physical properties predicted from the one-electron density. Similar $\Delta\rho$ features are present in both compounds. The redistribution of electron density indicated by the $\Delta\rho$ maps, which mainly reflects the effect of exchange interactions, does not support simple predictions from ionic and orbital models for the bonding in these structures. (I):